

# The dispersal of protoplanetary discs. – III: Influence of stellar mass on disc photoevaporation

Giovanni Picogna,<sup>1</sup>   \* Ercolano Barbara,<sup>1,2</sup>  Catherine C. Espaillat<sup>3</sup> 

<sup>1</sup>Universitäts-Sternwarte, Ludwig-Maximilians-Universität München, Scheinerstr. 1, D-81679 München, Germany

<sup>2</sup>Excellence Cluster Origins, Boltzmannstrasse 2, D-85748 Garching bei München, Germany

<sup>3</sup>Department of Astronomy & Institute for Astrophysical Research, Boston University, 725 Commonwealth Avenue, Boston, MA 02215, USA

Accepted XXX. Received YYY; in original form ZZZ

## ABSTRACT

The strong X-ray irradiation from young solar-type stars may play a crucial role in the thermodynamics and chemistry of circumstellar discs, driving their evolution in the last stages of disc dispersal as well as shaping the atmospheres of newborn planets. In this paper we study the influence of stellar mass on circumstellar disc mass-loss rates due to X-ray irradiation, extending our previous study of the mass-loss rate’s dependence on the X-ray luminosity and spectrum hardness. We focus on stars with masses between 0.1 and 1  $M_{\odot}$ , which are the main target of current and future missions to find potentially habitable planets. We find a linear relationship between the mass-loss rates and the stellar masses when changing the X-ray luminosity accordingly with the stellar mass. This linear increase is observed also when the X-ray luminosity is kept fixed because of the lower disc aspect ratio which allows the X-ray irradiation to reach larger radii. We provide new analytical relations for the mass-loss rates and profiles of photoevaporative winds as a function of the stellar mass that can be used in disc and planet population synthesis models. Our photoevaporative models correctly predict the observed trend of inner-disc lifetime as a function of stellar mass with an increased steepness for stars smaller than 0.3  $M_{\odot}$ , indicating that X-ray photoevaporation is a good candidate to explain the observed disc dispersal process.

**Key words:** accretion, accretion discs – protoplanetary discs – circumstellar matter – stars: pre-main-sequence – stars: winds, outflows – X-rays: stars.

## 1 INTRODUCTION

Our understanding of the physical processes driving the evolution of protoplanetary discs and ultimately the formation of planets is based on the observational evidence of disc lifetimes. Strom et al. (1989) found that accretion discs are ubiquitous around young stellar objects ( $\sim 1$  Myr). The initial disc fraction is almost independent of stellar mass (from 0.1 up to 10  $M_{\odot}$ ) and stellar environment (Lada et al. 2000, Bouy et al. 2006). After 10 Myr the picture changes completely since more than 90 % of stars show no emission within 1 au (Mamajek et al. 2004), and emission from small grains is found only in a few per cent of discs (Liu et al. 2004, Carpenter et al. 2005, Silverstone et al. 2006). This sets an upper limit to the disc dispersal process within 10 to 20 Myr (Hernández et al. 2007, Fedele et al. 2010, Ribas et al. 2014). Moreover, fitting the fraction of discs with dust emission at different wavelengths, Ribas et al. (2014) found an e-folding time of (2 to 3) Myr at (3 to 12)  $\mu\text{m}$  and (4 to 6) Myr at (22 to 24)  $\mu\text{m}$ , hinting at an inside-out dispersal of proto-planetary discs or to a second generation dust production (see also Koepferl et al. 2013). The dust disc lifetime as a function of the stellar mass is less well characterised but the dispersal timescale appears to be up to two times faster for high mass stars ( $\geq 2 M_{\odot}$ , Ribas et al. 2015). The mass accretion onto the central star has also been studied extensively,

though its evolution is less well constrained. Nevertheless, it has been shown that the characteristic timescale of disc accretion is shorter than that of dust disc dispersal (Jayawardhana et al. 2006, Fedele et al. 2010), and the accretion rate falls off as a function of time with a power law (e.g., Manara et al. 2012, Antonucci et al. 2014, Hartmann et al. 2016).

The main physical process driving disc dispersal is still largely unconstrained, and it might change during the disc evolution and at different locations in the disc. A large body of evidence is pointing at magnetic disc winds as the main mechanism responsible for angular momentum transfer and mass-loss (Bai 2016), particularly at early times. Photoevaporative disc winds may also co-exist at early times and perhaps dominate at later stages (Ercolano & Pascucci 2017; Weber et al. 2020). From a theoretical standpoint, there is a push to obtain better models that can be linked to observables to test their validity.

In the first paper of this series (Picogna et al. 2019, hereafter Paper I) we showed the dependence between the stellar X-ray luminosity and the mass-loss rate due to thermal winds generated by the XEUV heating from the central star. Then we studied the influence of carbon depletion (Wölfer et al. 2019) and stellar spectra hardness on the mass-loss rates (Ercolano et al. 2021, hereafter Paper II). In this following work, we focus on stellar mass dependence and how it might influence disc evolution.

In Section 2 we briefly discuss the numerical set-up adopted,

\* E-mail: picogna@usm.lmu.de

following our previous work. We then describe the main results in Section 3 and discuss their theoretical and observational implications in Section 4. The main conclusions are then drawn in Section 5.

## 2 METHODS

We run a series of hydrodynamical simulations following the approach outlined in Paper I that we briefly describe here for completeness.

The initial set-up is based on the gas densities and dust temperatures from the hydrostatic disc models from the D’Alessio Irradiated Accretion Disk (DIAD) radiative transfer models (D’Alessio et al. 1998, 1999, 2001, 2005, 2006), that best fit the median spectral energy distribution (SED) in Taurus. For this particular study a different set-up is adopted for each individual stellar mass, based on its mass and bolometric luminosity (see Figure 1). The stellar parameters were obtained from Siess et al. (2000) for an age of 1 Myr, and a metallicity  $Z = 0.02$  without overshooting.

We then ran the gas photoionization and dust radiative transfer code MOCASSIN (Ercolano et al. 2003, 2005, 2008), that solves the heating and cooling terms for various physical and irradiation properties at thermal equilibrium, to obtain a temperature prescription in the upper layers of the discs when irradiated by an X(EUV) stellar spectrum. We adopted X-ray luminosities scaled as a function of stellar mass following Güdel et al. (2007)

$$\log_{10}(L_X) = (1.54 \pm 0.12) \log_{10}(M_\star) + (30.31 \mp 0.06), \quad (1)$$

although a recent analysis by Flaischlen et al. (2021) found a steeper dependence.

The temperature prescription is shown in Figure 2 for the different spectral hardness (from Spec29 corresponding to  $10^{29}$  erg s<sup>-1</sup> to Spec31 equal to  $10^{31}$  erg s<sup>-1</sup>) following Paper II. It relates the local gas temperature to the column density to the central star (from  $5 \times 10^{20}$  pp cm<sup>-2</sup> to  $2 \times 10^{22}$  pp cm<sup>-2</sup>), and the local ionization parameter (Tarter et al. 1969)

$$\xi = \frac{L_X}{nr^2}, \quad (2)$$

where  $L_X$  is the X-ray luminosity,  $n$  the number density, and  $r$  the spherical radius from the central star. We compared it for completeness with the previously derived temperature prescription (used in Paper I) obtained for a star with  $L_X = 2 \times 10^{30}$  erg s<sup>-1</sup> in Ercolano et al. (2008).

Finally we ran a set of hydrodynamical simulations with a modified version of the PLUTO code (Mignone et al. 2007) presented in Paper I, in order to use the temperature prescription from MOCASSIN for column densities lower than the maximum penetration depth of X-rays ( $\sim 2 \times 10^{22}$  pp cm<sup>-2</sup>), and a perfect coupling between gas and dust temperatures using the DIAD models for larger column densities. We evolve the models until a steady state is reached for the disc structure and the gas streamlines in the wind.

We modelled 4 different stellar masses, ranging from  $0.1 M_\odot$  to  $1 M_\odot$  which, together with the  $0.7 M_\odot$  studied in Paper I, allow us to study in detail the stellar mass dependence on the mass-loss rates due to photoevaporative winds in T Tauri stars. The initial parameters adopted in the different runs are summarised in Table 1.

### 2.1 Hydrodynamical model

We adopted a spherical coordinate system centred on the star. The grid is logarithmically spaced in the radial direction with 500 cells,

in order to have better resolution in the inner region of the disc ( $R_{\text{in}} = 0.5 R_g$ ), where photoevaporation is mostly effective. At the same time, it allows us to model the disc out to large radii ( $R_{\text{out}} = 600$  au) without strongly increasing our computational costs and preventing boundary effects that can affect the stability of the wind flow. For a detailed discussion of the numerical artefacts induced by the grid outer boundary, the reader is referred to Paper I. The grid is spaced linearly in the polar direction, with a refinement at the wind launching region (100 cells from 0.01 to 0.5 rad, 200 cells from 0.5 to 1 rad, and 50 cells from 1 to  $\pi/2$  rad).

We initially evolve the system for few orbits at 10 au without stellar irradiation in order for it to readjust to the hydrostatic equilibrium. Then, we switch on the stellar heating (applied through a parameterisation as explained above and in Paper I) and continue to evolve the system for a few hundred orbits until the cumulative mass-loss rate and gas streamline in the wind have reached a steady-state after few hundred orbital periods (at 10 au), as shown in Figure 3.

## 3 RESULTS

There are two main locations that are of central importance in the study of photoevaporative winds.

(i) The gravitational radius  $R_g$ , which defines the location where a gas parcel becomes unbound from the central star, equating the sound speed to the Keplerian speed (Hollenbach et al. 1994, Liffman 2003).

$$\begin{aligned} R_g &= \frac{GM_\star}{c_s^2} = \frac{\gamma - 1}{2\gamma} \frac{GM_\star \mu m_H}{k_B T_0} \\ &\simeq 5.05 \left( \frac{T_0}{10^4 \text{ K}} \right)^{-1} \left( \frac{M_\star}{1 M_\odot} \right) [\text{au}], \end{aligned} \quad (3)$$

where  $\gamma = 5/3$  is the adiabatic index,  $G$  the gravitational constant,  $M_\star$  the stellar mass,  $\mu = 2.35$  the mean molecular weight,  $m_H$  the proton mass,  $k_B$  the Boltzmann constant, and  $T_0$  is the temperature at the base of the flow, which is equal to  $10^4$  K for a pure EUV wind. Owen et al. (2012) found analytically that the temperature in the flow should be fixed to first order by the stellar mass and thus be scale free when scaled by the gravitational radius. Thus we will scale in our analysis always (when not differently stated) the winds by this value, in order to study differences in the expected behaviour. We have to keep in mind that, since we are not treating an isothermal wind, the gravitational radius will not be a fixed cylindrical radius but an area where the temperature will increase due to X-ray irradiation winning over the gravitational pull from the central star. Nevertheless for simplicity in the rest of the paper we will refer to  $R_g$  assuming a fixed temperature of  $10^4$  K, typical of a isothermal EUV wind.

(ii) The critical radius  $R_c$ , which defines the location where the gas becomes supersonic, and for a Parker wind is

$$R_c = \frac{GM_\star}{2c_s^2}, \quad (4)$$

where  $c_s$  is the gas sound speed. The main assumptions of a Parker wind are that the outflow is steady, spherically symmetric and isothermal. Each streamline of the thermal wind will pass through its critical radius, forming a sonic surface which is fundamental in order to understand the properties of the photoevaporative wind. When we have the density and sound speed at the sonic surface we can determine the mass-flux in the entire flow as mass-flux is conserved (Begelman et al. 1983, Owen et al. 2012).

In this section we first discuss the effects of the irradiation from different stellar masses (and relative X-ray luminosities) on the global

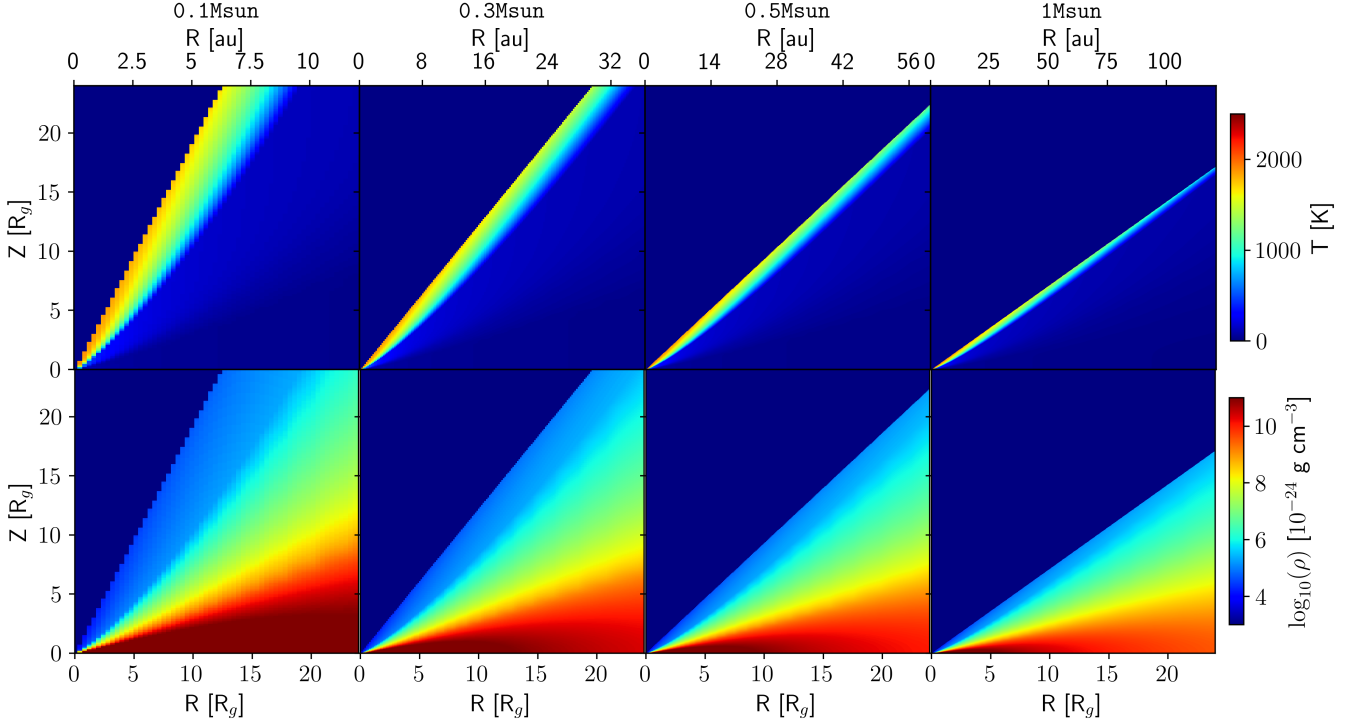


**Figure 1.** Initial dust temperature (upper panel) and density (lower panel) distribution in the inner 25 gravitational radii for the different runs from the DIAD models.

**Table 1.** Star and disc properties

Name	$M_{\star} [M_{\odot}]$	$R_{\star} [R_{\odot}]$	ST	$L_{\star} [L_{\odot}]$	$L_X [10^{29} \text{ erg s}^{-1}]$	$T_{\star} [\text{K}]$	$M_d [M_{\odot}]$	$R_{in} [\text{au}]$	Spectrum
1Msun	1.0	2.615	K6	2.335	20.4	4278	0.0444	0.445	Spec30
0.5Msun	0.5	2.125	M1	0.9288	7.02	3771	0.0363	0.2225	Spec30
0.3Msun	0.3	2.310	M5	0.6887	3.20	3360	0.0292	0.1335	Spec29
0.1Msun	0.1	1.055	M6	0.0856	0.59	2928	0.0264	0.0445	Spec29

mass loss rates and the radial mass loss profiles obtained at steady state from our 2D hydrodynamic calculations. In the second part we isolate the effect of changing only the stellar mass (keeping fixed the X-ray luminosity) and compare it with previous studies.

### 3.1 Disc profiles

We show in Figure 4 the gas temperature (top panel) and density (bottom panel) distribution for the different stellar masses at equilibrium. Two main aspects can be seen in the observed profiles. (i) The disc aspect ratio is strongly dependant on the stellar mass, and it is not affected by X-ray photoevaporation (comparing the bottom panels of Figures 4 and 1), as the X-rays cannot reach the deeper dense regions of the disc until the mass accretion rate becomes comparable to the photoevaporative mass-loss rate. We show this in a more quantitative way in Figure 5, where we plot the disc aspect ratio as a function of radius for the different stellar masses. Within  $40 R_g$  the disc flaring changes from  $0.1 M_{\odot}$  with a disc aspect ratio of  $h/r = 0.096 \cdot r^{0.25}$  to  $1 M_{\odot}$  with  $h/r = 0.036 \cdot r^{0.3}$ . The larger disc flaring for low stellar masses affects the vertical location of the maximum penetration depth of X-rays (shown in Figure 4 as a red dashed line) which shifts further away from the disc mid-plane. (ii) The temperature structure in the wind region, even when rescaled by

the gravitational radius, varies considerably for the different stellar masses, in contrast to what is predicted analytically in Owen et al. (2012), showing warmer winds for larger stellar masses and X-ray luminosities.

### 3.2 Mass-loss rates

We integrated the gas flow along the streamlines in the wind during the last 50 orbits of each simulation and plotted the resulting cumulative mass-loss rates as a function of stellar masses in a square-box plot in Figure 6, where we included also the run with a  $0.7 M_{\odot}$  star from Paper I, which has been rescaled in order to have the same stellar mass–X-ray luminosity adopted in these runs following equation 1. A fitting function has been overplotted with a dashed line, which shows the linear dependence of the mass-loss rate as a function of stellar mass. This linear trend is in contrast with the flat distribution as a function of stellar mass ( $\propto M_{\star}^{-0.068}$ ) obtained by Owen et al. (2012), but there the X-ray luminosity was kept constant while changing the stellar mass (see Section 3.4 for a detailed comparison). Furthermore, the linear trend does not show the flattening of the mass-loss rates observed for large X-ray luminosity in Paper I because even the  $1 M_{\odot}$  star has an X-ray luminosity of  $\log(L_X) = 30.3$ , which is smaller than the saturation value observed in the previous study. The best

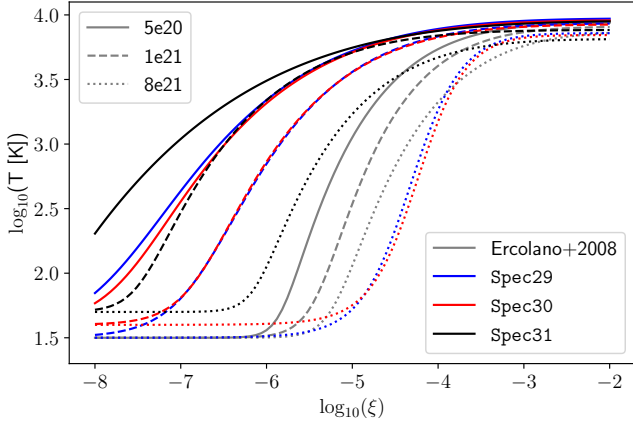


**Figure 2.** Temperature as a function of the ionization parameter, where 3 selected column densities are highlighted (Paper II). Three different spectral hardness are shown based on the stellar X-ray luminosity, from Spec29 corresponding to  $10^{29}$  erg s $^{-1}$  to Spec31 equal to  $10^{31}$  erg s $^{-1}$ .

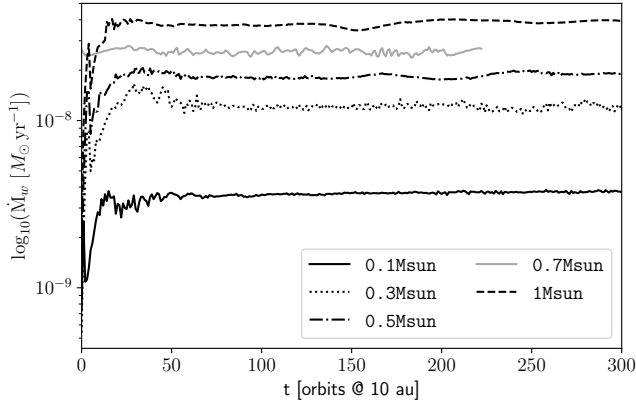


**Figure 3.** Cumulative mass-loss rate evolution as a function of time for the different stellar mass models. We included with a dark grey solid line the  $0.7 M_{\odot}$  run from Paper I, rescaled to have the same X-ray luminosity from equation 1.

fitting function obtained from the current study is

$$\dot{M}_w = 3.93 \times 10^{-8} \left( \frac{M_{\star}}{M_{\odot}} \right) [M_{\odot} \text{ yr}^{-1}]. \quad (5)$$

### 3.3 Wind profiles

From the derivative of the integrated mass-loss profile along the cylindrical radius we obtain the radial distribution of the mass-loss rate shown in Figure 7. Looking at the top panel, two trends are visible. There is an increase of the peak location as a function of stellar mass, with the only exception for the  $0.3 M_{\odot}$  star. A similar increase is seen in the maximum reach of the wind in the outer regions of the protoplanetary disc, which is able to remove material up to  $\sim 35$  au for a  $0.1 M_{\odot}$  star, while it reaches  $\sim 270$  au for a  $1 M_{\odot}$  star. This is a direct result of the lower flaring for disc orbiting larger mass stars, which allows the wind to have a further reach in the outer disc regions and generate a more massive wind.

To understand the anomaly observed for the  $0.3 M_{\odot}$  star we

rescaled the cylindrical radius by the gravitational radius in the bottom panel of Figure 7. We can see that, when rescaled, we obtain 2 similar profiles for the low X-ray luminosities (and spectra hardness) and two for the high luminosities. This can be explained with the harder spectra in the ‘soft’ X-ray band (0.1–1 keV) for lower X-ray luminosities which drives the peak at larger radii, as studied in Paper II. The relative difference amongst the profiles, once rescaled, is given by a combined effect of the change in the stellar mass and absolute value of the X-ray luminosity.

The best fit for the surface mass-loss rate is given by the following function, as in Paper I

$$\begin{aligned} \dot{\Sigma}_w(R) = \ln(10) & \left( \frac{6a \ln(R)^5}{R \ln(10)^6} + \frac{5b \ln(R)^4}{R \ln(10)^5} + \frac{4c \ln(R)^3}{R \ln(10)^4} + \right. \\ & \left. \frac{3d \ln(R)^2}{R \ln(10)^3} + \frac{2e \ln(R)}{R \ln(10)^2} + \right. \\ & \left. \frac{f}{R \ln(10)} \right) \frac{\dot{M}_w(R)}{2\pi R} [M_{\odot} \text{ au}^{-2} \text{ yr}^{-1}] \end{aligned} \quad (6)$$

where

$$\frac{\dot{M}_w(R)}{\dot{M}_w(L_X)} = 10^{a \log R^6 + b \log R^5 + c \log R^4 + d \log R^3 + e \log R^2 + f \log R + g} \quad (7)$$

where the parameters for the different stellar masses are given in Table 2.

### 3.4 Stellar mass dependence

In order to isolate the effect of stellar mass on the photoevaporative mass-loss rates we performed a new set of simulations where we fixed the X-ray luminosity to the value of  $7 \times 10^{29}$  erg s $^{-1}$  (i.e. that of the  $0.5 M_{\odot}$  star). We show in Figure 8 the cumulative mass-loss rate for the different stellar masses and we compare it with the prescription from Owen et al. (2012). We see that the mass-loss rate is not independent of the stellar mass, in contrast to what observed in Owen et al. (2012). However, the dependence on the stellar mass becomes much more shallow, increasing only by a factor 3 from  $0.1 M_{\odot}$  to  $1 M_{\odot}$  instead of an order of magnitude as shown in Figure 6. The linear fit that matches the data shown in Figure 8 is

$$\dot{M}_w = 2.34 \times 10^{-8} \left( \frac{M_{\star}}{M_{\odot}} \right) + 6.23 \times 10^{-9} [M_{\odot} \text{ yr}^{-1}]. \quad (8)$$

To understand the origin of the stellar mass dependence we plotted in Figure 9 the Surface mass-loss rate as a function of cylindrical radius for the different runs, which shows two main trends. An increase in the peak location and in the maximum reach as a function of stellar mass. The increased peak location is a direct consequence of the larger gravitational pull for more massive stars, which affects the location where eventually a gap will open in the disc. Although it scales linearly with stellar mass, it has little influence on the cumulative mass-loss rate since the disc mass scales as the square of the distance from the central star and the contribution from within the gravitational radius is negligible. Moreover Paper I have shown that the cumulative mass-loss rate is insensitive to the inner hole radius for holes up to 30 au for a  $0.7 M_{\odot}$  star. The increased reach of the stellar irradiation is the main effect driving up the mass-loss rates, since for intermediate cylindrical radii the profiles are lying one on top of each other. The reason why the runs with larger mass stars have a further reach is purely geometrical, since flatter discs allow the radiation to reach larger cylindrical radii before being absorbed. The change in the disc flaring as a function of stellar mass comes from the increase in the stellar bolometric luminosity (affecting the



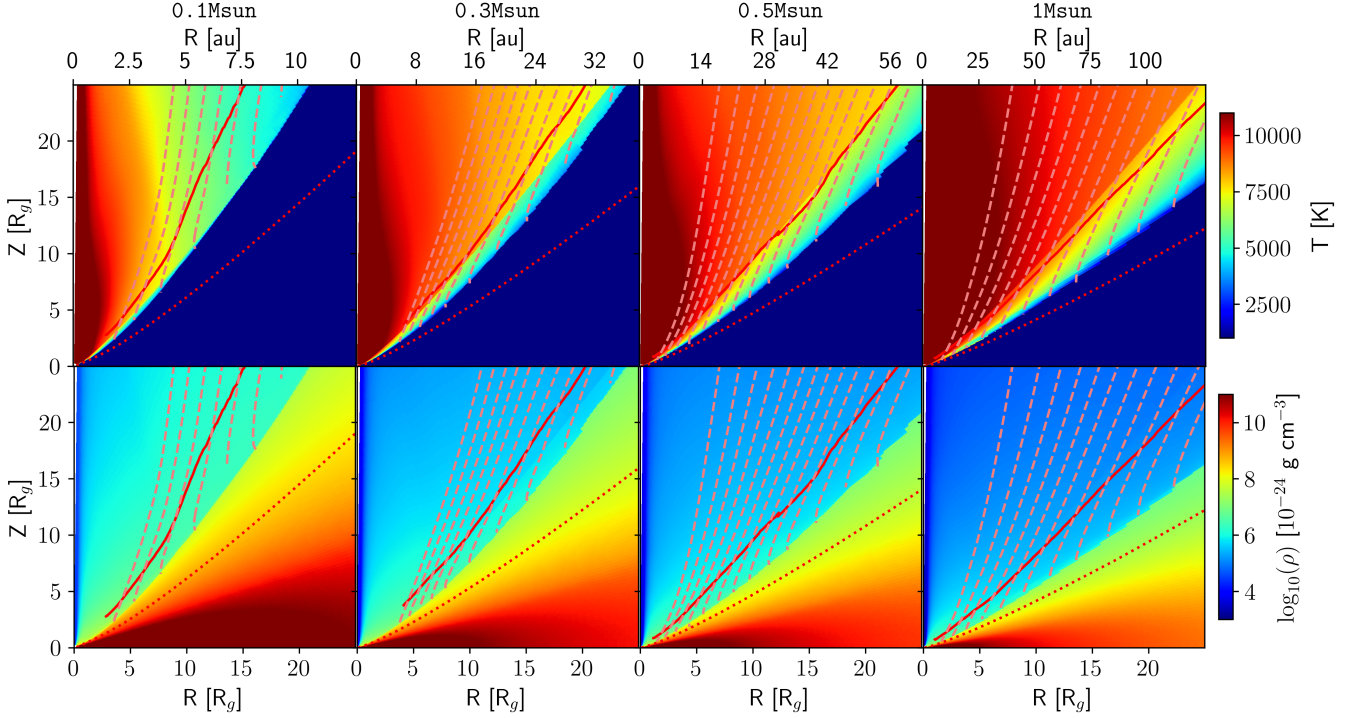


**Figure 4.** Temperature (upper panel) and density (lower panel) distribution in the inner 25 gravitational radii for the different runs. The sonic surface is overlaid with a solid red line and the gas streamlines every 5% of the cumulative mass-loss rate with orange dashed lines. The maximum penetration depth of the X-rays is shown as well with a dashed red line.

**Table 2.** Parameters for the Surface density profiles in equations 6,7

$M_\star [M_\odot]$	a	b	c	d	e	f	g	$\dot{M}_w [10^{-8} M_\odot \text{yr}^{-1}]$
1.0	-0.6344	6.3587	-26.1445	56.4477	-67.7403	43.9212	-13.2316	3.86446
0.5	-1.2320	10.8505	-38.6939	71.2489	-71.4279	37.8707	-9.3508	1.9046
0.3	-1.3206	13.0475	-53.6990	117.6027	-144.3769	94.7854	-26.7363	1.17156
0.1	-3.8337	22.9100	-55.1282	67.8919	-45.0138	16.2977	-3.5426	0.37588

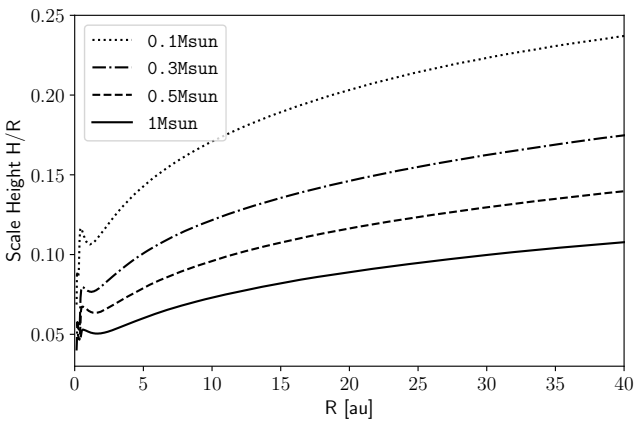


**Figure 5.** Initial disc aspect ratio for the runs reported in Tab. 1.

dust temperature) and in the disc mass from the DIAD models (see Table 1).

Besides the change in the disc flaring, another difference between the runs (see Table 1) is the disc mass. The bulk of the disc mass

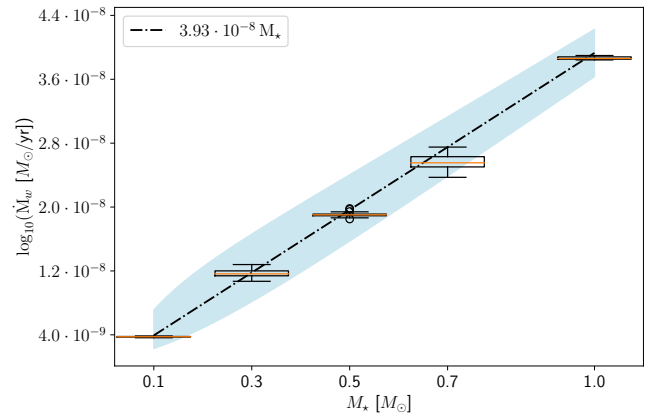


**Figure 6.** Box plot of the cumulative mass-loss rate as a function of stellar mass over the last 50 orbital timescales at 10 au. The derived linear fit is overlotted with a black dashed line, and a blue shaded region shows the variation in the mass-loss rate due to the uncertainty in the X-ray luminosity as a function of stellar mass in equation 1.

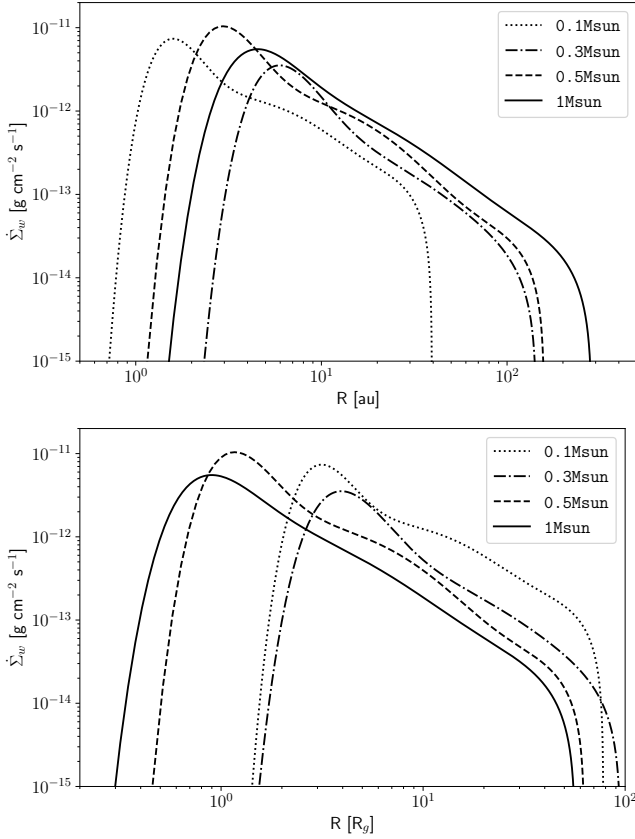


**Figure 7.** Surface density mass-loss rate profile for the different simulations. In the top panel the mass-loss rate is plotted as a function of the cylindrical radius in au, while in the bottom panel the dependence is a function of the gravitational radius (see section 3.3).

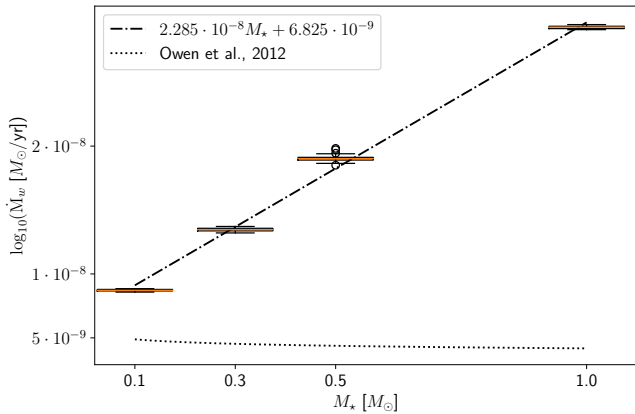


**Figure 8.** Box plot of the cumulative mass-loss rate as a function of stellar mass over the last 50 orbital timescales at 10 au, keeping the X-ray luminosity fixed. A linear fit has been overplotted with a dot-dashed line, as well as the prediction from (Owen et al. 2012) in a dotted line.

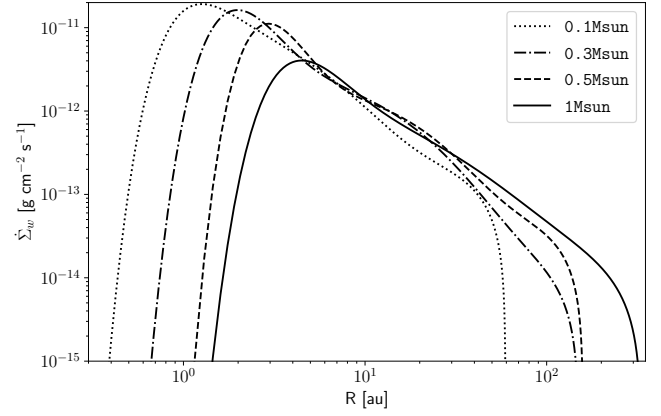


**Figure 9.** Surface density mass-loss rate profile as a function of cylindrical radius for the different simulations at fixed X-ray luminosity.

resides in the disc mid-plane which is not reachable by the stellar irradiation. However changing the disc mass affects the disc structure and thus the height at which the irradiation can penetrate. Owen et al. (2012) found out that a variation in the disc mass was not changing the cumulative mass-loss rate, and more recently we confirmed this result in Wölfer et al. (2019, see their Figure 7) where we saw a wind mass-loss rate independent of the disc mass for a large range of disc-to-star mass ratios and carbon abundances. We are thus confident that, at this stage of disc evolution, the disc mass is not affecting the cumulative wind mass-loss rate.

## 4 DISCUSSION

In this section we discuss the differences between the properties at the sonic surface in our model in comparison with the theoretical prediction for a Parker wind and previous numerical results. We then compare the inner-disc lifetime obtained from our model with observationally derived one.

### 4.1 Sonic surface

The local gas properties at the sonic surface are fundamental to understand the overall wind properties. For a disc wind, the sound speed at the sonic surface should be on the same order of magnitude of the Parker value which, from equation 4, is

$$c_s^2 \approx \frac{GM_\star}{2R}. \quad (9)$$

In Figure 10 we plot the density (upper plot) and temperature (bottom plot) at the sonic surface for the different runs, and we compare the temperature with the theoretical prediction for a Parker wind. We see that in our case the steepness of the temperature profile is much shallow, and only the  $1 M_\odot$  star (green line) matches the expected profile between 3 and 6 gravitational radii before flattening again. This behaviour has been observed also by Owen et al. 2012 (see their Figure 6), where the Parker wind value was recovered only around the gravitational radius, flattening close to the star and far away from it, following the sigmoidal temperature prescription coming from Figure 2. Two trends can be identified in Figure 10. (i) The density at the sonic surface is almost linearly increasing with stellar mass, being  $9.2 \times 10^{-17} \text{ g cm}^{-3}$  for the  $0.1 M_\odot$  star and  $6.5 \times 10^{-18} \text{ g cm}^{-3}$  for  $1 M_\odot$ . The bump observed inside  $1 R_g$  is caused by the bump in the

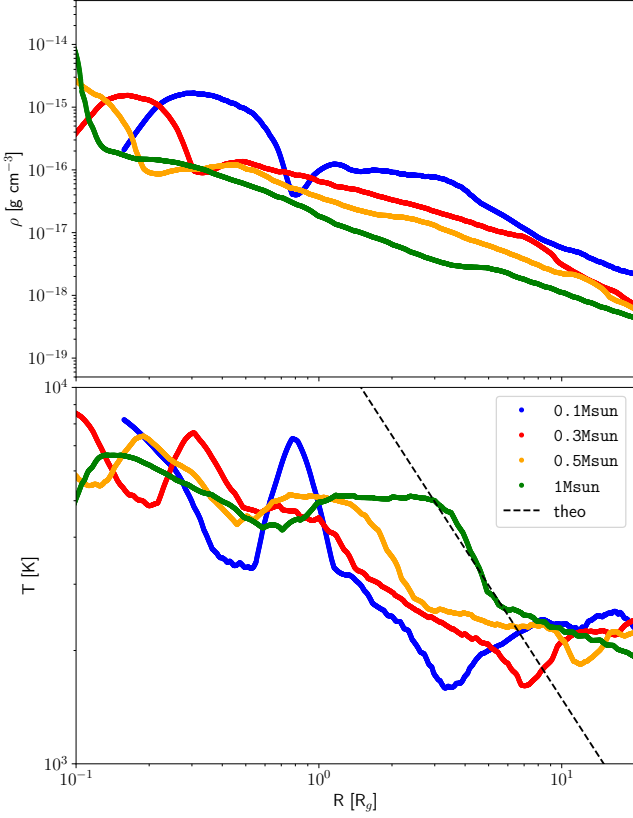


**Figure 10.** Temperature at the sonic surface as a function of the gravitational radius for the different stellar masses modelled.

disc scale height from Figure 5, which comes directly from the DIAD models and is caused by an increase of the dust temperatures close to the star. (ii) The temperature passes through a transition regime with a similar slope which is shifted towards the central star going from the higher to the lower mass star. This shift is also linearly increasing with the stellar mass, and to show it, we replot the bottom panel of Figure 10 dividing the gravitational radius again by the stellar mass in Figure 11, where the theoretical temperature for the  $1 M_{\odot}$  star is reported to guide the eye. The linear radial shift in the temperature at the sonic surface may be due to the difference in the disc scale height, which affects the density at the sonic surface, and thus the ionization parameter which is responsible for the change in the temperature.

## 4.2 Observational constraints

The observed lifetimes of discs around stars of different masses presents a fundamental constraint for disc dispersal models. Our new models which span the observational range of observed stellar masses in disc surveys allow us to make the first such comparison for a disc-dispersal model.

We can define the inner-disc lifetime  $t_{\text{life}}$  as the time at which accretion rates  $\dot{M}_{\text{acc}}$  decrease to photoevaporative rates  $\dot{M}_w$ . This happens because, at this time, a gap opens in the inner disc (around the gravitational radius) disconnecting the inner and outer disc evolution. The inner disc disperses on a short timescale (viscous timescale at few au), not being replenished anymore by the outer disc. The lifetime

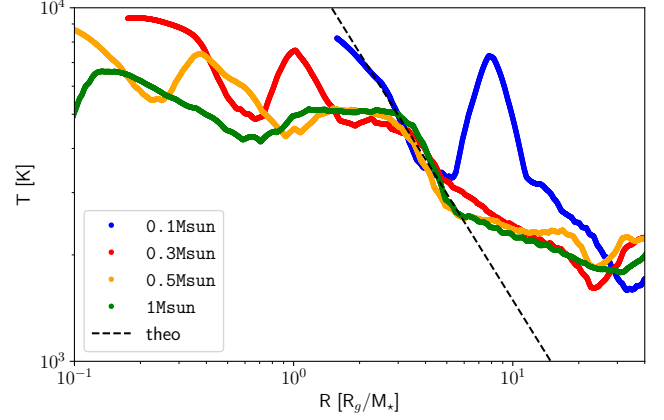


**Figure 11.** Temperature at sonic surface as a function of the gravitational radius divided by the stellar mass for the different models.

of the inner disc  $t_{\text{life}}$  can be approximated then by

$$\dot{M}_w = \dot{M}_{\text{acc},0} \left( \frac{t_{\text{life}}}{t_{\nu}} \right)^{-3/2}, \quad (10)$$

where  $t_{\nu}$  is the viscous timescale

$$t_{\nu} = \frac{M_{\text{disc},0}}{2\dot{M}_{\text{acc},0}}. \quad (11)$$

Combining the previous equations we obtain

$$\begin{aligned} t_{\text{life}} &= t_{\nu} \left( \frac{\dot{M}_{\text{acc},0}}{\dot{M}_w} \right)^{2/3} = \frac{M_{\text{disc},0}}{2\dot{M}_{\text{acc}}} \left( \frac{\dot{M}_{\text{acc}}}{\dot{M}_w} \right)^{2/3} \\ &= \frac{1}{2} \left( \frac{M_{\text{disc},0}}{\dot{M}_{\text{acc},0}^{1/3} \dot{M}_w^{2/3}} \right), \end{aligned} \quad (12)$$

where the free parameters are given by the initial disc mass and accretion rates.

For several star forming regions an observational  $\dot{M}_{\text{acc}} - M_{\star}$  relation has been determined (Alcalá et al. 2017, Manara et al. 2017, Flaischlen et al. 2021, Alcalá et al. 2021), where, like in the 1 to 3 Myr old Lupus, a sharp increase of the accretion rate is observed for low-mass stars ( $< 0.2 M_{\odot}$ , Alcalá et al. 2017)

$$\log(\dot{M}_{\text{acc}}) = \begin{cases} 4.58(\pm 0.68) \log(M_{\star}) - 6.11(\mp 0.61), & \leq 0.2 M_{\odot} \\ 1.37(\pm 0.24) \log(M_{\star}) - 8.46(\mp 0.11), & \text{otherwise.} \end{cases} \quad (13)$$

We can then use the current accretion rates to determine the initial accretion rate, assuming a constant disc viscous evolution

$$\dot{M}_{\text{acc}} = \dot{M}_{\text{acc},0} \left( \frac{t}{t_{\nu}} \right)^{-3/2}, \quad (14)$$

which leaves us only with the free parameter of the initial disc mass  $M_{\text{disc},0}$ .

An interesting star forming region to test the validity of our observational predictions is  $\lambda$  Ori (also known as Collinder 69), since it has been extensively studied in X-ray emission (Barrado et al. 2011), and it seems to be at a critical age for disc dissipation ( $\sim 5$  Myr). Bayo et al. 2012 obtained the cumulative disc fraction as a function of stellar mass from infrared excess observations of this open cluster, and we can convert this into an approximate inner-disc lifetime,

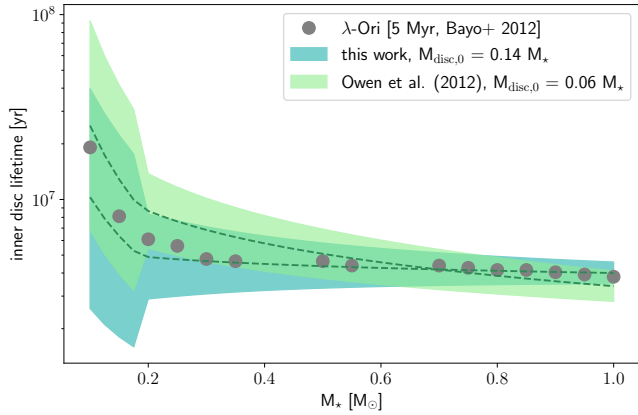


**Figure 12.** Inner-disc lifetime calculated from our models using equation 12 compared with the disc fraction as a function of the mass for the members of  $\lambda$  Ori. The shaded regions show the uncertainty in equations 13,1.

following the approach of Komaki et al. 2021 as

$$t_{\text{life}} \simeq -\frac{t_{\text{age}}}{\ln f_{\text{disc}}}, \quad (15)$$

where  $t_{\text{age}} = 5$  Myr (Bayo et al. 2011).

In Figure 12 we directly compared the observational data points derived from Bayo et al. (2012) in grey, with the inner-disc lifetime obtained from eqs. 5, 12 in sea-green and, for comparison, in light-green the result using the photoevaporative mass-loss rate from equation B1 of Owen et al. (2012). The shaded region represents the uncertainty in the observational relation between the accretion rates and stellar masses (equation 13) and that in the X-ray luminosity as a function of stellar mass (equation 1). The sharp increase of the shaded regions for stars  $< 0.2 M_{\odot}$  is mainly caused by the large uncertainty of equation 13 for small mass stars.

In order to get the best fit to the observation we used a linear relation between the initial disc mass and stellar mass and a initial value of  $0.14 M_{\star}$  for the current models and  $0.06 M_{\star}$  for Owen et al. (2012). Andrews et al. (2013) found a roughly linear relationship between the disc mass and stellar mass, studying a large sample of Class II discs. More recently Pascucci et al. (2016), studying a few young star forming regions, found a slightly steeper than linear dust disc mass - stellar mass relationship, though including in the sample also the brown dwarfs linearizes it again (Rilinger & Espaillat 2021). The results match very well the observations for the whole range of explored masses, and in particular the change in the slope for masses below  $0.3 M_{\odot}$ , which gives us confidence on the ability of the photoevaporative models to predict the observed inner-disc lifetimes. Furthermore, our new prescription, with a linear scaling of disc masses as a function of stellar mass, captures better the observed distribution with respect to the previous state of the art model.

The gap opening condition is local and it is usually satisfied in late stages of disc evolution inside 10 au (see e.g. Paper I). Adopting the cumulative wind mass-loss rate in equation 12 is a simplification, although the mass removed in the outer disc affects the mass flux reaching the inner disc. We are currently working to merge all our results in comprehensive disc and planet population synthesis models (Emsenhuber et al. in prep., Küster et al. in prep.), but this simplified approach allows us nevertheless to test whether our models correctly predicts the observed behaviour.

## 5 CONCLUSIONS

We have computed for the first time comprehensive photoevaporation models spanning the whole observed range of low mass stars ( $\leq 1 M_{\odot}$ ) using observationally derived X-ray stellar spectra. We found that

- (i) stellar mass and bolometric luminosity have a strong impact on the underlying disc structure, changing its aspect ratio (see Figures 1,5). As a result, on the one hand the X-ray irradiation can penetrate deeper into the disc for smaller mass stars, generating denser and colder winds (see Figures 4,10). On the other hand, the flatter discs around high mass stars allow the stellar irradiation to reach larger radii and generate more massive winds (see Figure 3);
- (ii) we provide fitting functions in Table 2 for the surface mass-loss rate profiles for different stellar masses whose luminosity is scaled based on equation 1 that can be readily applied to disc and planet population synthesis codes;
- (iii) the resulting cumulative mass loss rate scales linearly with the stellar mass (see equation 5);
- (iv) the temperature as a function of the gravitational radius at the sonic surface scales linearly with the stellar mass (see Figure 11);
- (v) the observed inner-disc lifetimes as a function of stellar mass can be very well reproduced by our new models, indicating that X-ray photoevaporation dominates the final phases of protoplanetary disc evolution (see Figure 12).

## 6 DATA AVAILABILITY

The data underlying this article and the scripts used to create the Figures are available at <https://cutt.ly/IEIY9JI>.

## ACKNOWLEDGEMENTS

We thank the anonymous referee for a thorough report and insightful suggestions which improved the paper. GP acknowledges support from the DFG Research Unit ‘Transition Disks’ (FOR 2634/2). This work was performed on the computing facilities of the Computational Center for Particle and Astrophysics (C2PAP). GP would like to thank Kristina Monsch and Tommaso Grassi for their insightful comments on the manuscript and during the development of the project. This research was supported by the Excellence Cluster ORIGINS which is funded by the Deutsche Forschungsgemeinschaft (DFG, German Research Foundation) under Germany’s Excellence Strategy - EXC-2094 - 390783311. This paper utilizes the D’Alessio Irradiated Accretion Disk (DIAD) code. We wish to recognize the work of Paola D’Alessio, who passed away in 2013. Her legacy and pioneering work live on through her substantial contributions to the field.

## REFERENCES

- Alcalá J. M., et al., 2017, *A&A*, **600**, A20
- Alcalá J. M., et al., 2021, *A&A*, **652**, A72
- Andrews S. M., Rosenfeld K. A., Kraus A. L., Wilner D. J., 2013, *ApJ*, **771**, 129
- Antonucci S., García López R., Nisini B., Caratti o Garatti A., Giannini T., Lorenzetti D., 2014, *A&A*, **572**, A62
- Bai X.-N., 2016, *ApJ*, **821**, 80
- Barrado D., et al., 2011, *A&A*, **526**, A21
- Bayo A., et al., 2011, *A&A*, **536**, A63



- Bayo A., Barrado D., Huéramo N., Morales-Calderón M., Melo C., Stauffer J., Stelzer B., 2012, *A&A*, 547, A80
- Begelman M. C., McKee C. F., Shields G. A., 1983, *ApJ*, 271, 70
- Bouy H., Martín E. L., Brandner W., Zapatero-Osorio M. R., Béjar V. J. S., Schirmer M., Huéramo N., Ghez A. M., 2006, *A&A*, 451, 177
- Carpenter J. M., Wolf S., Schreyer K., Launhardt R., Henning T., 2005, *AJ*, 129, 1049
- D'Alessio P., Cantó J., Calvet N., Lizano S., 1998, *ApJ*, 500, 411
- D'Alessio P., Calvet N., Hartmann L., Lizano S., Cantó J., 1999, *ApJ*, 527, 893
- D'Alessio P., Calvet N., Hartmann L., 2001, *ApJ*, 553, 321
- D'Alessio P., et al., 2005, *ApJ*, 621, 461
- D'Alessio P., Calvet N., Hartmann L., Franco-Hernández R., Servín H., 2006, *ApJ*, 638, 314
- Ercolano B., Pascucci I., 2017, *Royal Society Open Science*, 4, 170114
- Ercolano B., Barlow M. J., Storey P. J., Liu X. W., 2003, *MNRAS*, 340, 1136
- Ercolano B., Barlow M. J., Storey P. J., 2005, *MNRAS*, 362, 1038
- Ercolano B., Young P. R., Drake J. J., Raymond J. C., 2008, *ApJS*, 175, 534
- Ercolano B., Picogna G., Monsch K., Drake J. J., Preibisch T., 2021, *MNRAS*, Fedele D., van den Ancker M. E., Henning T., Jayawardhana R., Oliveira J. M., 2010, *A&A*, 510, A72
- Flaischlen S., Preibisch T., Manara C. F., Ercolano B., 2021, *A&A*, 648, A121
- Güdel M., et al., 2007, *A&A*, 468, 353
- Hartmann L., Herczeg G., Calvet N., 2016, *ARA&A*, 54, 135
- Hernández J., et al., 2007, *ApJ*, 671, 1784
- Hollenbach D., Johnstone D., Lizano S., Shu F., 1994, *ApJ*, 428, 654
- Jayawardhana R., Coffey J., Scholz A., Brandeker A., van Kerkwijk M. H., 2006, *ApJ*, 648, 1206
- Koepferl C. M., Ercolano B., Dale J., Teixeira P. S., Ratzka T., Spezzi L., 2013, *MNRAS*, 428, 3327
- Komaki A., Nakatani R., Yoshida N., 2021, *ApJ*, 910, 51
- Lada C. J., Muench A. A., Haisch Karl E. J., Lada E. A., Alves J. F., Tollestrup E. V., Willner S. P., 2000, *AJ*, 120, 3162
- Liffman K., 2003, *Publ. Astron. Soc. Australia*, 20, 337
- Liu M. C., Matthews B. C., Williams J. P., Kalas P. G., 2004, *ApJ*, 608, 526
- Mamajek E. E., Meyer M. R., Hinz P. M., Hoffmann W. F., Cohen M., Hora J. L., 2004, *ApJ*, 612, 496
- Manara C. F., Robberto M., Da Rio N., Lodato G., Hillenbrand L. A., Stassun K. G., Soderblom D. R., 2012, *ApJ*, 755, 154
- Manara C. F., et al., 2017, *A&A*, 604, A127
- Mignone A., Bodo G., Massaglia S., Matsakos T., Tesileanu O., Zanni C., Ferrari A., 2007, *ApJS*, 170, 228
- Owen J. E., Clarke C. J., Ercolano B., 2012, *MNRAS*, 422, 1880
- Pascucci I., et al., 2016, *ApJ*, 831, 125
- Picogna G., Ercolano B., Owen J. E., Weber M. L., 2019, *MNRAS*, 487, 691
- Ribas Á., Merín B., Bouy H., Maud L. T., 2014, *A&A*, 561, A54
- Ribas Á., Bouy H., Merín B., 2015, *A&A*, 576, A52
- Rilinger A. M., Espaillat C. C., 2021, arXiv e-prints, p. arXiv:2106.05247
- Siess L., Dufour E., Forestini M., 2000, *A&A*, 358, 593
- Silverstone M. D., et al., 2006, *ApJ*, 639, 1138
- Strom K. M., Strom S. E., Edwards S., Cabrit S., Skrutskie M. F., 1989, *AJ*, 97, 1451
- Tarter C. B., Tucker W. H., Salpeter E. E., 1969, *ApJ*, 156, 943
- Weber M. L., Ercolano B., Picogna G., Hartmann L., Rodenkirch P. J., 2020, *MNRAS*, 496, 223
- Wölfer L., Picogna G., Ercolano B., van Dishoeck E. F., 2019, *MNRAS*, 490, 5596

This paper has been typeset from a  $\text{\LaTeX}$  file prepared by the author.